Response of a shell structure subject to distributed harmonic excitation

Rui Cao, J. Stuart Bolton

Ray W. Herrick Laboratories, Mechanical Engineering, Purdue University
177 S. Russell Street, West Lafayette, IN, USA, 47907

Email: cao101@purdue.edu

Abstract. Previously, a coupled, two-dimensional structural-acoustic ring model was constructed to simulate the dynamic and acoustical behavior of pneumatic tires. Analytical forced solutions were obtained and were experimentally verified through laser velocimeter measurement made using automobile tires. However, the two-dimensional ring model is incapable of representing higher order, in-plane modal motion in either the circumferential or axial directions. Therefore, in this paper, a three-dimensional pressurized circular shell model is proposed to study the in-plane shearing motion and the effect of different forcing conditions. Closed form analytical solutions were obtained for both free and forced vibrations of the shell under simply supported boundary conditions. Dispersion relations were calculated and different wave types were identified by their different speeds. Shell surface mobility results under various input distributions were also studied and compared. Spatial Fourier series decompositions were also performed on the spatial mobility results to give the forced dispersion relations, which illustrate clearly the influence of input force spatial distribution. Such a model has practical application in identifying the sources of noise and vibration problems in automotive tires.

1. Introduction

Many analytical ring models [1-3] have been developed to simulate tire vibrations and some can also allow for coupling of the air cavity with the structural vibration to predict the acoustical resonances [4]. These ring models can be effective in predicting the radial and circumferential motions of the tire; however they cannot represent the transverse modal motion in the tire axial direction and thus are insufficient to account for tire-width-related effects. Such width-related behavior may be an important factor in influencing tire acoustic performance. Thus, shell models have been applied to represent tire vibration more completely. A free and forced vibration analysis of a rotating shell by Kim and Bolton [5] revealed the wave types traveling in the thin shell and the effect of rotation. Molisani el al. [6] proposed a simple coupled tire/cavity shell model which made modal analysis possible. Kim and Bolton [7] were also the first to use the traveling wave finite element method to calculate the dispersion relations in tire structures. Later, Waki at al. further developed the traveling wave finite element method and they were able to calculate the forced response of a tire [8]. Sabiniarz and Kropp [9] used their finite element tire model to show that in-plane shearing motion could occur in the tire treadband due to tire sidewall vibration. This later motion is of particular interest since its cut on frequency falls within the frequency range where the tire horn effect is most prominent and so it could account for a significant portion of tire-related vehicle pass by noise.

Accurate vibration simulation results can provide structural modal information, which can be helpful in the identification of the mechanism of the above-mentioned in-plane shearing motion, for example.

Content from this work may be used under the terms of the Creative Commons Attribution 3.0 licence. Any further distribution of this work must maintain attribution to the author(s) and the title of the work, journal citation and DOI.
Published under licence by IOP Publishing Ltd

The forced vibration response can also give the surface velocity of the structure and thus may provide input for tire noise radiation predictions. With the intention of describing higher order in-plane motions in tire treadbands, the transverse and in-plane motion across the width direction in a simplified finite-width cylindrical shell is investigated here. But note that due to the material property variance, the resonance frequency and response amplitude may not precisely match the measurement results from real tires. Also, the forced response to inputs having different spatial distributions, i.e., point excitation, line excitation and area excitation, are compared to see how the shell model response depends on input force shape and how various wave types are enhanced or suppressed by changing the spatial distribution of the input force.

2. Model description

Here, a thin shell model was used to investigate the in-plane shearing phenomenon that has been observed in tire treadbands and sidewalls. Also, different input excitations were applied on the shell to study how the shell response depends on various excitation conditions.

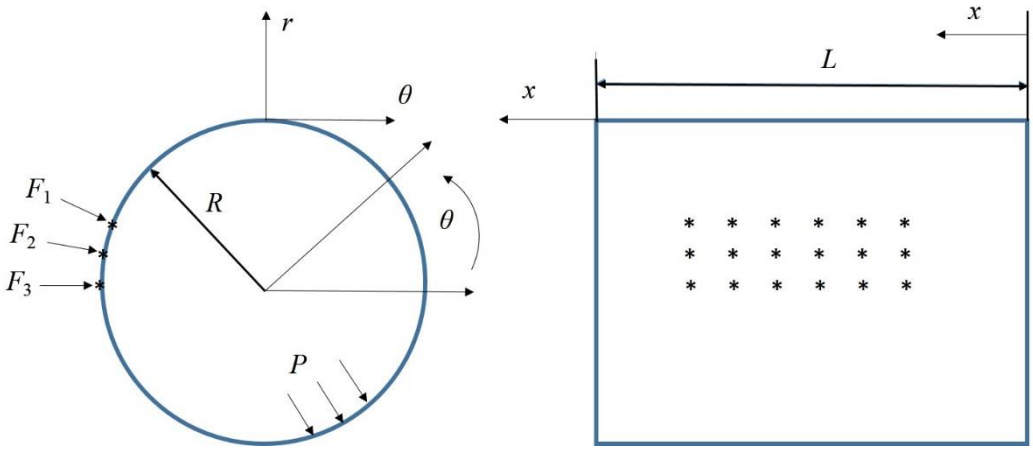

Figure 1. Simply supported shell.

The cylindrical shell is as shown in Figure 1 with radius R and width L. Here u_r, u_θ and u_x are the displacements of the shell in the radial, tangential and axial directions, respectively. Internal pressure, P, is applied to the inner surface of the cylindrical shell which has the effect of stiffening it in the circumferential direction. External point forces can be applied anywhere on the shell and the position and quantity of these forces can be modified to simulate point, line and area inputs.

The two edges of the cylindrical shell are simply supported in this case, which means that both radial and tangential motions at the edges are constrained to be zero; the axial motion, however, is unconstrained. Typically, the tire tread thickness-to-radius ratio is less than 0.1, which, according to Kang and Riedel's work [10], makes it reasonable to assume that the neutral plane coincides with the centroidal plane of the shell. So, thin shell theory is used here, where displacements in the tangential and axial direction vary linearly with thickness. The radial shear strain in this thin shell model is also neglected since shear waves in tires are not easily excited and have a very small influence on tire vibration response at frequencies below 4 KHz [11].

3. Free vibration

The free vibration of the pressurized thin cylindrical shell model is first calculated, which then provides the necessary modal information for forced response calculations. By following Soedel's thin shell theory [12], Love's equations give

$$L_x\left(u_x,u_\theta,u_r\right)=\rho h\frac{\partial^2 u_x}{\partial t^2} \quad (1)$$

$$L_\theta\left(u_x,u_\theta,u_r\right)=\rho h\frac{\partial^2 u_\theta}{\partial t^2} \quad (2)$$

$$L_r\left(u_x,u_\theta,u_r\right)=\rho h\frac{\partial^2 u_r}{\partial t^2} \quad (3)$$

where ρ is the density of the shell, h is the thickness of the shell and the linear differential operators are

$$L_x\left(u_x,u_\theta,u_r\right)=K\frac{\partial^2 u_x}{\partial x^2}+\frac{K(1-\nu)}{2R^2}\frac{\partial^2 u_x}{\partial\theta^2}+\frac{K(1+\nu)}{2R}\frac{\partial^2 u_\theta}{\partial x\partial\theta}+\nu\frac{K}{R}\frac{\partial u_r}{\partial x}+q_x \quad (4)$$

$$\begin{aligned}L_\theta\left(u_x,u_\theta,u_r\right)=&\frac{K(1+\nu)}{2R}\frac{\partial^2 u_x}{\partial x\partial\theta}+\frac{K(1-\nu)}{2}\frac{\partial^2 u_\theta}{\partial x^2}+\frac{K}{R^2}\frac{\partial^2 u_\theta}{\partial\theta^2}+\frac{D(1-\nu)}{2R^2}\frac{\partial^2 u_\theta}{\partial x^2}+\frac{D}{R^4}\frac{\partial^2 u_\theta}{\partial\theta^2}\\&\frac{K}{R^2}\frac{\partial u_r}{\partial\theta}+\frac{D}{R^2}\frac{\partial^3 u_r}{\partial x^2\partial\theta}-\frac{D}{R^4}\frac{\partial^3 u_r}{\partial\theta^3}+q_\theta\end{aligned} \quad (5)$$

$$\begin{aligned}L_r\left(u_x,u_\theta,u_r\right)=&-\frac{K\nu}{R}\frac{\partial u_x}{\partial x}-\frac{K}{R^2}\frac{\partial u_\theta}{\partial\theta}+\frac{D}{R^2}\frac{\partial^3 u_\theta}{\partial x^2\partial\theta}+\frac{D}{R^4}\frac{\partial^3 u_\theta}{\partial\theta^3}+N_{xx}^r\frac{\partial^2 u_r}{\partial x^2}+\frac{N_{\theta\theta}^r}{R^2}\frac{\partial^2 u_r}{\partial\theta^2}\\&+D\left(\frac{\partial^4 u_r}{\partial x^4}+\frac{1}{R^2}\frac{\partial^4 u_r}{\partial x^2\partial\theta^2}+\frac{1}{R^4}\frac{\partial^4 u_r}{\partial\theta^4}\right)-\frac{Ku_r}{R^2}+q_r\end{aligned} \quad (6)$$

among which, υ is the Poisson's ratio, D is the bending stiffness calculated as $Eh^3[12(1-\upsilon^2)]^{-1}$, K is the membrane stiffness calculated as Eh, E is the Young's modulus, q_x, q_θ, q_r are distributed forces in each direction and finally, $N_{\theta\theta}^r = PR$ is the in-plane force that results from the inflation pressure, P.

Table 1. Shell material properties and dimensions.

Parameter	Value	Parameter	Value
Radius R	0.332 [m]	Young's modulus E	4.8×10^8 [Pa]
Width L	0.215 [m]	Poisson's ratio υ	0.45
Thickness h	0.008 [m]	Hysteretic damping η	0.3
Density ρ	1200 [kg·m^{-3}]	Inflation pressure P	2.06×10^5 [Pa]

Since the cylindrical shell is simply-supported, the following boundary conditions apply:

$$u_r(0,\theta)=0, u_r(L,\theta)=0 \quad (7a, 7b)$$

$$u_\theta(0,\theta)=0, u_\theta(L,\theta)=0 \quad (8a, 8b)$$

$$M_{xx}(0,\theta)=0, M_{xx}(L,\theta)=0 \quad (9a, 9b)$$

$$N_{xx}(0,\theta)=0, N_{xx}(L,\theta)=0 \quad (10a, 10b)$$

where M_{xx} is the axial moment and N_{xx} is the axial shear force. The solutions that satisfy these boundary conditions have the form

$$u_x=A\cos\left(\frac{k_m\pi x}{L}\right)\cos\left(k_n\left(\theta-\phi\right)\right) \quad (11)$$

$$u_\theta=B\sin\left(\frac{k_m\pi x}{L}\right)\sin\left(k_n\left(\theta-\phi\right)\right) \quad (12)$$

$$u_r=C\sin\left(\frac{k_m\pi x}{L}\right)\cos\left(k_n\left(\theta-\phi\right)\right) \quad (13)$$

where k_m is the wavenumber in the width direction and k_n is the wavenumber in the circumferential direction. Next, those solutions are substituted into the equations of motion to obtain

$$\begin{bmatrix} \rho h\omega^2 - k_{11} & k_{12} & k_{13} \\ k_{21} & \rho h\omega^2 - k_{22} & k_{23} \\ k_{31} & k_{32} & \rho h\omega^2 - k_{33} \end{bmatrix} \begin{Bmatrix} A \\ B \\ C \end{Bmatrix} = 0 \quad (14)$$

where the k_{ij}'s are constants containing k_m, k_n and other material-related factors. By fixing the wavenumbers k_m and k_n, and then equating the determinant of Equation 14 to zero, it is possible to solve for the natural frequency associated with a given (m,n) mode. For each (m,n) mode, there will be 3 pairs of natural frequencies, representing a circumferential transverse wave, an axial longitudinal wave and a circumferential longitudinal wave. Given the calculated natural frequencies, it is also possible to work out the amplitude ratio between the different displacements. That is, the displacement of each mode can be expressed as

$$\begin{Bmatrix} u_{xmni} \\ u_{\theta mni} \\ u_{rmni} \end{Bmatrix} = C_{mni} \begin{Bmatrix} A_{mni} / C_{mni} \cos\left(\dfrac{k_m \pi x}{L}\right) \cos\left(k_n(\theta - \phi)\right) \\ B_{mni} / C_{mni} \sin\left(\dfrac{k_m \pi x}{L}\right) \sin\left(k_n(\theta - \phi)\right) \\ \sin\left(\dfrac{k_m \pi x}{L}\right) \cos\left(k_n(\theta - \phi)\right) \end{Bmatrix}. \quad (15)$$

4. Forced vibration

Once the natural frequencies are obtained, the free vibration modes can be combined with appropriate weighting to represent the total forced response. When following Soedel's [12] procedure, a modal participation factor η_{mni} is added to each mode: the result is

$$\sum_{m=1}^{N_1} \sum_{n=0}^{N_2} \left[\rho h \ddot{\eta}_{mni} + \rho h \omega_{mni}^2 \eta_{mni} \right] u_{mni} = q_i \quad (16)$$

where i = 1, 2, 3 denotes the modes in the axial, circumferential and radial directions, respectively. Here N_1 and N_2 represent the total numbers of modes considered in practice (which, in theory, go to infinity). We can adjust the values of N_1 and N_2 depending on the frequency range of interest. Next, each equation is multiplied by u_{pqi} on both sides to obtain

$$\sum_{m=1}^{N_1} \sum_{n=0}^{N_2} \left[\rho h \ddot{\eta}_{mni} + \rho h \omega_{mni}^2 \eta_{mni} \right] u_{mni} u_{pqi} = q_i u_{pqi} \quad (17)$$

and both sides of the above equation are integrated over the entire shell surface. Due to the orthogonality of the modes, terms not satisfying $p = m$, $q = n$ vanish, thus causing the integral equations to reduce to summations. Finally, the integrated equations for i = 1,2,3 can be added to calculate the modal participation factor as follows:

$$\rho h \left[\omega_{mni}^2 - \omega^2 \right] \eta_{mni} \int_0^L \int_0^{2\pi} \left(u_{xmni}^2 + u_{\theta mni}^2 + u_{rmni}^2 \right) R d\theta dx = \int_0^L \int_0^{2\pi} \left(q_x u_{xmni} + q_\theta u_{\theta mni} + q_r u_{rmni} \right) R d\theta dx \,. \quad (18)$$

Thus the modal participation factor can be easily calculated in this case. Then the modal force is:

$$F_{mni} = \int_0^L \int_0^{2\pi} \left(q_x u_{xmni} + q_\theta u_{\theta mni} + q_r u_{rmni} \right) R d\theta dx \,. \quad (19)$$

Note that the Young's modulus used in the calculation contains a hysteretic damping factor, which causes the natural frequencies to be complex. The latter ensures that the response of the shell remains finite when driven at one of the natural frequencies.

4.1. Modal summation for harmonic point excitation

With the obtained modal participation factor, the previously defined mode shape Equations 15 can be combined to calculate the resultant forced-displacement response in the axial, circumferential and radial

directions. However, instead of choosing an arbitrary phase, ϕ, in the assumed solutions (as in Equations 11 to 13), the solutions were expressed in the form of two orthogonal modes: i.e.,

$$u_{xmni(1)} = \frac{A_{mni}}{C_{mni}} \cos\left(\frac{k_m \pi x}{L}\right) \cos\left(k_n \theta\right), u_{xmni(2)} = \frac{A_{mni}}{C_{mni}} \cos\left(\frac{k_m \pi x}{L}\right) \sin\left(k_n \theta\right) \quad (20)$$

$$u_{\theta mni(1)} = \frac{A_{mni}}{C_{mni}} \sin\left(\frac{k_m \pi x}{L}\right) \sin\left(k_n \theta\right), u_{\theta mni(2)} = \frac{A_{mni}}{C_{mni}} \sin\left(\frac{k_m \pi x}{L}\right) \cos\left(k_n \theta\right) \quad (21)$$

$$u_{rmni(1)} = \frac{A_{mni}}{C_{mni}} \sin\left(\frac{k_m \pi x}{L}\right) \cos\left(k_n \theta\right), u_{rmni(2)} = \frac{A_{mni}}{C_{mni}} \sin\left(\frac{k_m \pi x}{L}\right) \sin\left(k_n \theta\right). \quad (22)$$

In the end, the solution should include components from both orthogonal modes, so the solutions are written as:

$$u_x = \sum_{i=1}^{3} \sum_{m=1}^{N_1} \sum_{n=0}^{N_2} \left(\eta_{mni(1)} u_{xmni(1)} + \eta_{mni(2)} u_{xmni(2)}\right) \quad (23)$$

$$u_\theta = \sum_{i=1}^{3} \sum_{m=1}^{N_1} \sum_{n=0}^{N_2} \left(\eta_{mni(1)} u_{\theta mni(1)} + \eta_{mni(2)} u_{\theta mni(2)}\right) \quad (24)$$

$$u_r = \sum_{i=1}^{3} \sum_{m=1}^{N_1} \sum_{n=0}^{N_2} \left(\eta_{mni(1)} u_{rmni(1)} + \eta_{mni(2)} u_{rmni(2)}\right). \quad (25)$$

4.2. Generic excitation

To force the system, multiple point excitations at arbitrary angles were used to represent a generic excitation case which could be reduced easily to a single point input or a line input. Many point excitations were used to simulate an area excitation by controlling the number of excitation points and the space between these points. In that case,

$$q_r = \sum_{p=1}^{FN_1} \sum_{q=1}^{FN_2} \frac{F_{rpq}}{R} \delta\left(x - x_p\right) \delta\left(\theta - \theta_q\right) \quad (26)$$

$$q_\theta = \sum_{p=1}^{FN_1} \sum_{q=1}^{FN_2} \frac{F_{\theta ij}}{R} \delta\left(x - x_p\right) \delta\left(\theta - \theta_q\right) \quad (27)$$

where FN_1 is the number of excitation points along the axial direction and FN_2 is the number of excitation points along the circumferential direction, F_{rpq} is the radial force amplitude at (x_p,θ_q) and $F_{\theta pq}$ is the tangential force amplitude at (x_p,θ_q). Although the input area is rectangular, different force amplitudes can be specified at each specific point location to create the required input distribution shape. For simplicity, the calculations in this paper were based on uniform force amplitudes applied at various excitation locations; only the input locations and number of excitation points were modified.

These excitation forces need to be substituted back into Equation 19 to calculate the modal forces. The Dirac delta function alters the integral to a summation over the total excitation points, which finally gives

$$F_{mni} = \sum_{p=1}^{FN_1} \sum_{q=1}^{FN_2} \left(F_r u_{xmni}(x_p, \theta_q) + F_\theta u_{\theta mni}(x_p, \theta_q)\right) \quad (28)$$

These modal forces then allow us to calculate the modal participation factors for different excitation conditions. Here, the single point excitation, axial line excitation and rectangular area excitation were considered.

5. Results

Both free vibration results and the forced vibration results will be given, based on the dimensions and the material properties of the shell given in Table 1. The total input force was given unity magnitude, so the resultant surface velocity has a value equal to the surface mobility.

5.1. Dispersion relations

The dispersion relations for all three types of wave were calculated and are shown in Figure 2, where the real part of the natural frequency is plotted against circumferential mode number, with axial mode number as a parameter. The family of circumferential bending waves cut on in a relatively low frequency range and travel at approximately the flexural wave speed (here, about 200 m/s). The axial longitudinal waves cut on in the medium frequency range due to the relatively low stiffness in the axial direction compared to that in the circumferential direction. Finally, the circumferential longitudinal waves cut on in a higher frequency range due to the relatively high stiffness in the circumferential direction resulting from both curvature and pretension, and these waves represent in-plane motion of the shell. Although no out-of-plane shearing waves are allowed for in this type of shell model, the in-plane circumferential motion varies in the width direction and the axial longitudinal motion varies in the circumferential direction, hence causing what is described here as in-plane shearing. The first branch of all the modes shown in Figure 2 were not incorporated into the forced response results since that type of motion is prevented by the boundary conditions. That is when $m = 1$, k_m is equal to 0 and so no motion can exist

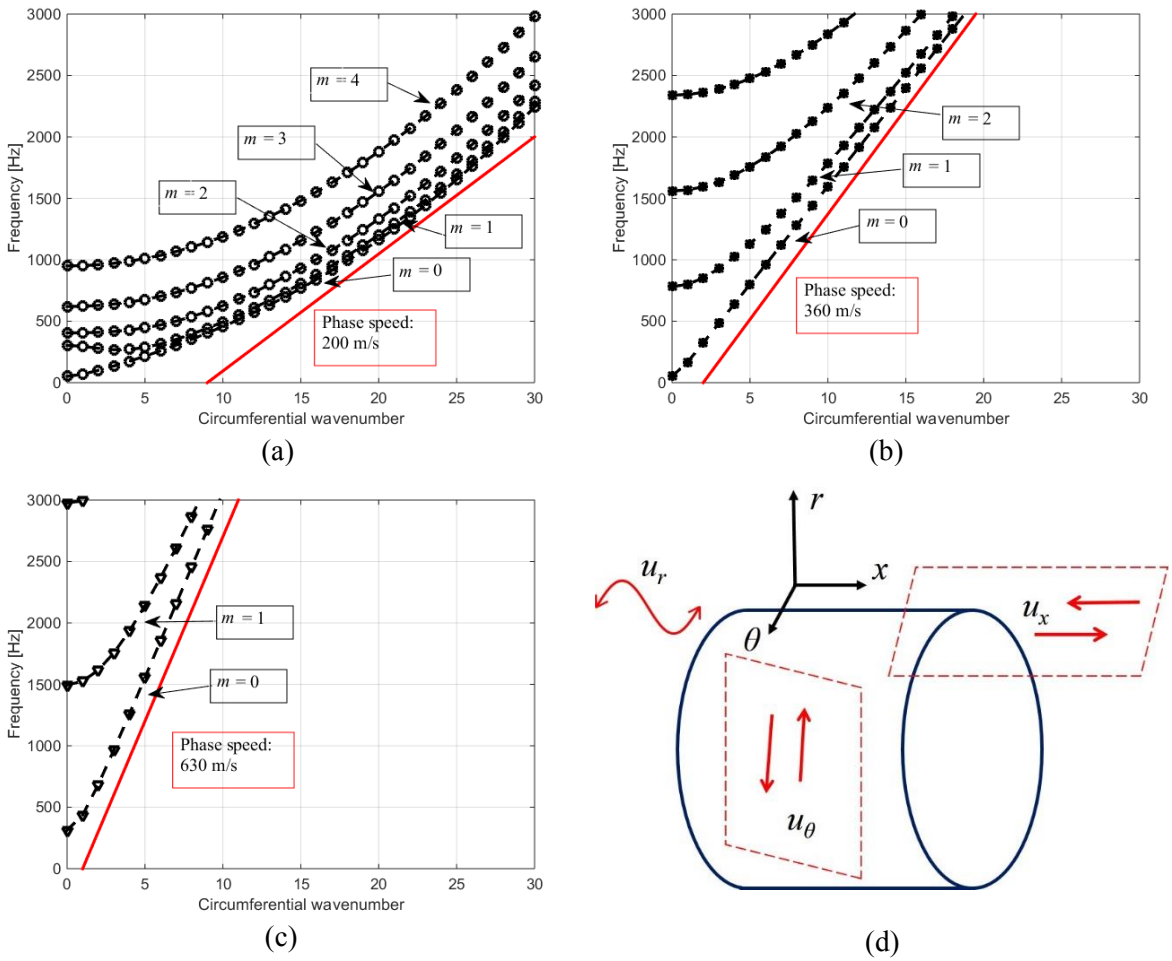

Figure 2. (a) Dispersion plot of circumferential bending wave; (b) Dispersion plot of axial longitudinal wave; (c) Dispersion plot of circumferential longitudinal wave; (d) Sketch of all three wave types.

in the radial and circumferential direction; in contrast, the axial direction motion is a constant. Thus, the simple support boundary condition does not allow the lowest wave modes to exist for the various wave types. However, such low frequency resonances are typical and prominent in tire structures as shown both experimentally and in simulation by Sabiniarz and Kropp [7]. So in the following forced vibration response, the mobility results are not similar in some respect to those from a tire due to lack of low frequency modes. Note that other boundary condition of the shell model could be considered in order to incorporate the low order modal motion, e.g. sliding boundary condition.

In Figure 2(d), the three wave types are illustrated: u_r represents the circumferential bending wave which has most of its displacement in the radial direction; u_θ represents the circumferential longitudinal wave, which travels tangentially in the θ-direction; and u_x represents the axial longitudinal wave, which propagates axially in the x-direction. The distinction between the wave types can be seen from the different phase speeds, with the circumferential longitudinal wave being the fastest, the axial longitudinal wave the second fastest and the circumferential bending wave being the slowest.

5.2. Mobility results

External forces were applied here to drive various structural modes. First, the radial input mobility and circumferential transfer mobility for a point excited shell were calculated, where the drive point was at $x = L/3.3$ and $\theta = 0$. The mobility was calculated at the midpoint in the axial direction along the shell circumference for the line input and area input cases. In the calculations shown in Figure 3, there was only a radial external force, while in the results shown in Figure 4, there were both radial and tangential external forces. Because of the coupling between radial and circumferential motion, the radially driven response still results in a finite circumferential mobility, but it is much smaller compared to the radial mobility. It can be seen in Figure 4 that after adding the tangential excitation, the circumferential mobility is significantly increased while the radial mobility is essentially unchanged.

In addition, the spatial radial mobility, that is the radial mobility plotted along the shell circumference center-line, is shown in Figure 5 for radial point, line and area excitations, respectively. The point excitation is the same as stated above; the excitation line is axial and spans from $L/8$ to $7L/8$ with 20 points in between, and the area excitation is square-like with 20 points spanning from $L/8$ to $7L/8$ axially and 20 points spanning from $-\pi/6$ to $\pi/6$ circumferentially. By comparing the results shown in Figure 5, it is clear that the point excitation is most effective at exciting all modes and that the area excitation limits the modal response to a much lower frequency range, and the response remains local to the excitation area. Such phenomenon can be considered to result from applying a window in the spatial domain and the windowing effect can be seen in the dispersion results presented in the next section.

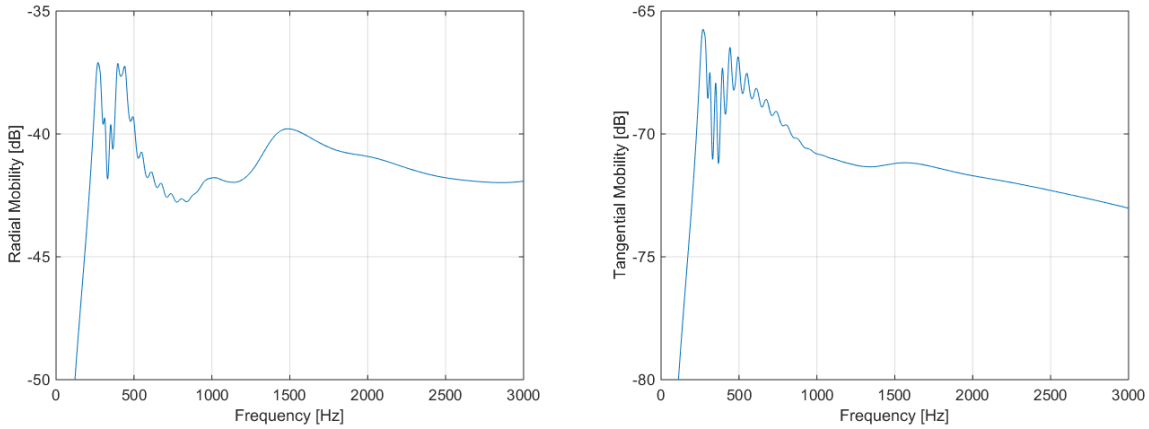

(a) (b)

Figure 3. (a) Radial input mobility under radial point excitation; (b) Circumferential transfer mobility under radial point excitation (close to the excitation location). Reference mobility 1 *m*/*s*/*N*.

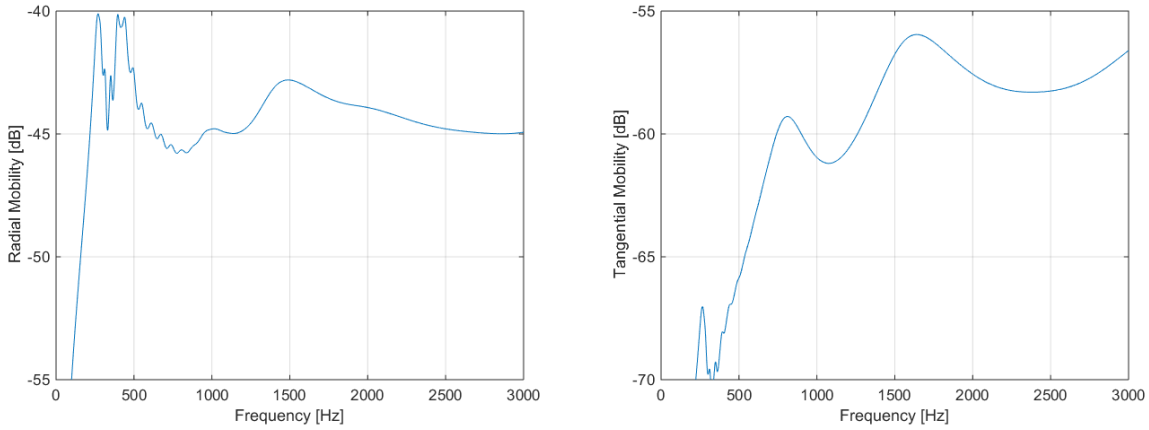

(a) (b)

Figure 4. (a) Radial input mobility under combined radial and tangential point excitation; (b) Circumferential input mobility under combined radial and tangential point excitation. Reference mobility 1 *m*/*s*/*N*.

As for the tangential mobility results shown in Figure 6(a) as a function of width at the driving point, a distinctive nodal line around 1500 Hz, which is associated with the cut on of the 2nd branch of the circumferential longitudinal wave in Figure 2(c), which has one node in the width direction. It can also

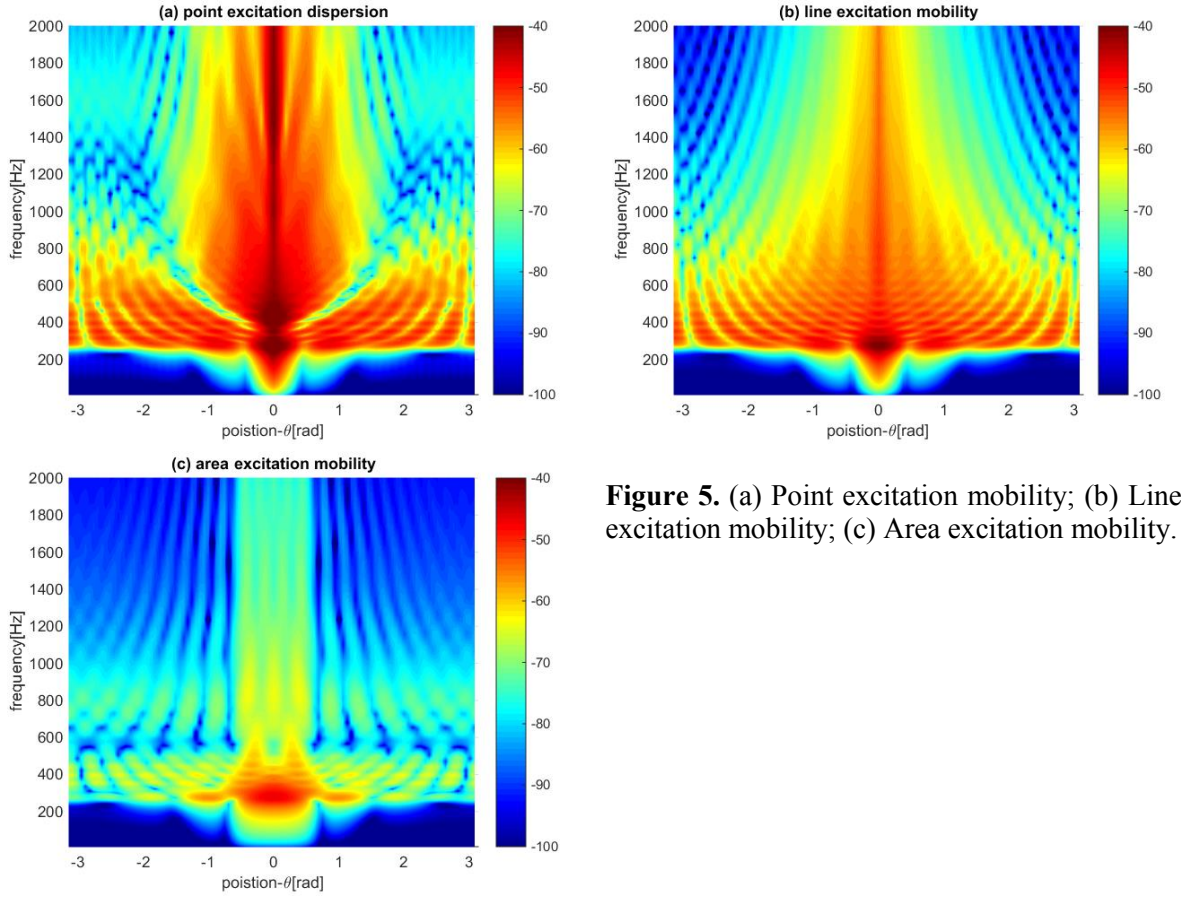

Figure 5. (a) Point excitation mobility; (b) Line excitation mobility; (c) Area excitation mobility.

be seen in Figure 6(b) that tangential excitation can also trigger axial longitudinal waves due to the coupling in the shell. From 800 Hz to 1600 Hz, the 2nd branch of the axial longitudinal waves in Figure 2(b) is the dominant propagating mode, where there is also one node in the width direction: see Figure

6(b). But starting from 1600 Hz, the 3rd branch of the axial wave cuts on and now two nodes appear in the axial direction.

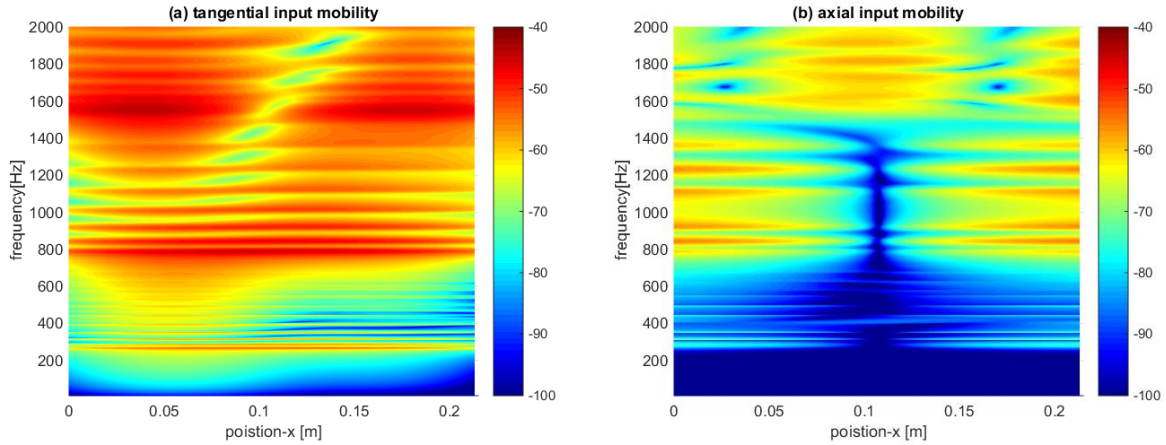

Figure 6. (a) Tangential input mobility due to tangential point excitation; (b) Axial mobility due to tangential point excitation.

5.3. Dispersion results

By performing a Fourier series decomposition of the previous spatial mobility results, the frequency-wavenumber results are obtained, as shown in Figure 7. In this representation, it is very clear that the point excitation drives the most modes while the line excitation only effectively excited the $m = 1$ mode circumferential bending wave: i.e., the line excitation does not couple effectively with higher order

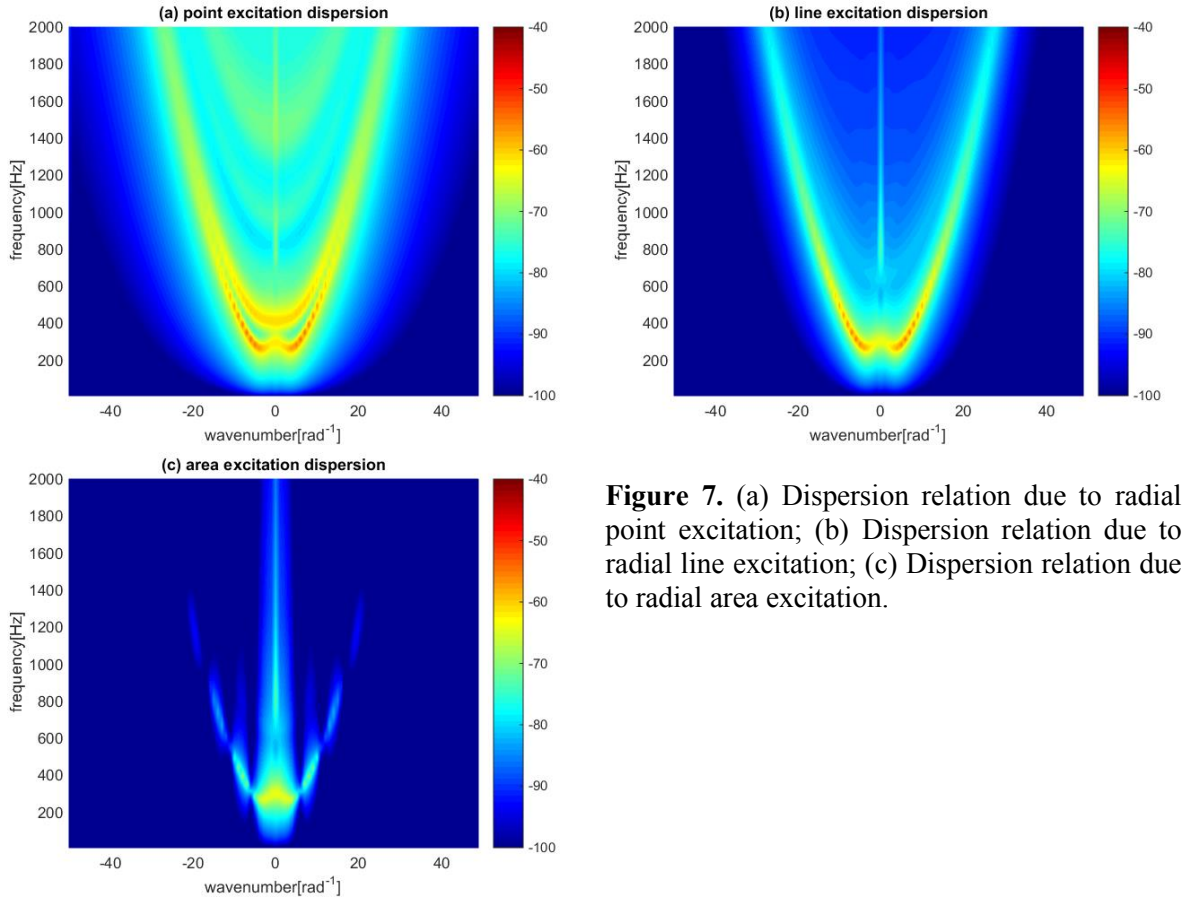

Figure 7. (a) Dispersion relation due to radial point excitation; (b) Dispersion relation due to radial line excitation; (c) Dispersion relation due to radial area excitation.

cross-sectional modes. The area excitation further suppresses both axial and circumferential resonances from the cylindrical shell structure. Note that the vertical strips in Figure 7(c) result from the rectangular nature of the force "window." It was evident from the previous mobility results that the larger the excitation area, the lower the modal the response would be. Taken together, these results demonstrate that the spatial distribution of the input force has a very large impact on the nature of the cylinder's response in terms of wave types. This observation in turn suggests that the sound radiation from the cylinder can be controlled by tailoring the spatial distribution of the input force.

Although the results presented here show various interesting phenomenon, they do not precisely match the real tire tread response mainly due to the boundary conditions considered here. Further study is required to modify the shell boundary conditions to stiffness-supported at both edges in order to simulate more realistic tire tread vibration.

6. Conclusion

From this investigation, it can be observed that in-plane shearing both in the circumferential and axial directions play a significant role in the finite-width shell response. The circumferential shearing is due to the changing mode shape in the axial direction and the axial shearing is due to the changing mode shape in the circumferential direction. Also, different spatial excitation results were compared and the excitation area distribution creates a spatial domain windowing effect, which can suppress certain modes and wave types in the forced response.

In vehicle tires, various structural waves can propagate in the shell-like treadband. The above-mentioned types of waves can be an important part of the waves traveling in the tire treadband and so they could act as the sources for tire noise in different frequency range. So the identification and control of these waves can be an important aspect in controlling tire noise issues.

References

[1] L. E. Kung, W. Soedel and T. Y. Yang, "Free vibration of a pneumatic tire-wheel unit using a ring on an elastic foundation and a finite element model." *Journal of Sound and Vibration*, 107.2 (1986): 181-194.

[2] P. Kindt, P. Sas,and W. Desmet, "Development and validation of a three-dimensional ring-based structural tyre model." *Journal of Sound and Vibration*, 326.3 (2009): 852-869.

[3] W. Kropp, "Structure-borne sound on a smooth tyre." *Applied Acoustics* 26(3) (1989): 181-192.

[4] R. Cao and J. S. Bolton, "Improved Model for Coupled Structural-Acoustic Modes of Tires." *SAE International Journal of Passenger Cars-Mechanical Systems*, 8.2015-01-2199 (2015): 845-854.

[5] Y-J. Kim and J. S. Bolton, "Effects of rotation on the dynamics of a circular cylindrical shell with application to tire vibration." *Journal of Sound and Vibration*, 275.3 (2004): 605-621.

[6] L. R. Molisani, R. A. Burdisso and D. Tsihlas, "A coupled tire structure/acoustic cavity model." *International Journal of Solids and Structures*, 40 (2003): 5125-5138.

[7] Y.J. Kim and J. S. Bolton, "Analysis of tire vibration by using a hybrid two-dimensional finite element based on composite shell theory," *Proceedings of INTER-NOISE 2003*, paper N294, 8 pages, Seogwipo, South Korea, August 2003

[8] Y. Waki, B. R. Mace and M. J. Brennan. "Free and forced vibrations of a tyre using a wave/finite element approach." *Journal of Sound and Vibration* 323.3 (2009): 737-756.

[9] P. Sabiniarz and W. Kropp. "A waveguide finite element aided analysis of the wave field on a stationary tyre, not in contact with the ground." *Journal of Sound and Vibration*, 329.15 (2010): 3041-3064.

[10] B. Kang and C. H. Riedel. "On the validity of planar, thick curved beam models derived with respect to centroidal and neutral axes." *Wave Motion*, 49.1 (2012): 1-23.

[11] R. J Pinnington and A. R. Briscoe. "A wave model for a pneumatic tyre belt." *Journal of Sound and Vibration*, 253.5 (2002): 941-959.

[12] W. Soedel, Vibrations of Shells and Plates. *CRC Press*, 2004.